Structural characterisation of Cu-Zr thin film combinatorial libraries with synchrotron radiation at the limit of crystallinity

B. Putz [a,b,1,*], O. Milkovič [c,d,1], G. Mohanty [a,e,1], R. Ipach [a], L. Pethö [a], J. Milkovičová [c,h], X. Maeder [a], T.E.J. Edwards [a], P. Schweizer [a], M. Coduri [g], K. Saksl [c,f,h], J. Michler [a]

[a] Empa, Swiss Federal Laboratories for Materials Science and Technology, Laboratory for Mechanics of Materials and Nanostructures, Feuerwerkerstrasse 39, 3602 Thun, Switzerland
[b] Department of Materials Science, Montanuniversitaet Leoben, Franz Josef Straße 18, A-8700 Leoben, Austria
[c] Institute of Materials Research, Slovak Academy of Sciences, Watsonova 47, 040 01 Košice, Slovakia
[d] Institute of Experimental Physics, Slovak Academy of Sciences, Watsonova 47, 040 01 Košice, Slovakia
[e] Materials Science and Environmental Engineering, Faculty of Engineering and Natural Sciences, Tampere University, 33014 Tampere, Finland
[f] Faculty of Science, Institute of Physics, Pavol Jozef Šafárik University in Košice, 041 80 Košice, Slovakia
[g] Department of Chemistry, University of Pavia, Viale Taramelli 16, 27100 Pavia, Italy
[h] Institute of Materials and Quality Engineering, Faculty of Materials, Metallurgy and Recycling, Technical University of Košice, Letná 9, Košice 042 00, Slovakia

HIGHLIGHTS

- Novel high throughput methodology to understand atomistic structure of thin film metallic glass combinatorial libraries on polymer substrates.
- Co-sputtered CuZr films exhibit dual-phase microstructure that could not be produced by conventional methods according to the CuZr phase diagram.
- Linear phase ratio between amorphous $Cu_{51}Zr_{14}$ and nanocrystalline α-Zr as a function Zr content (25–80 at%), forming a mechanical mixture.
- Real space HR-STEM analyses of representative composition substantiate XRD results.

GRAPHICAL ABSTRACT
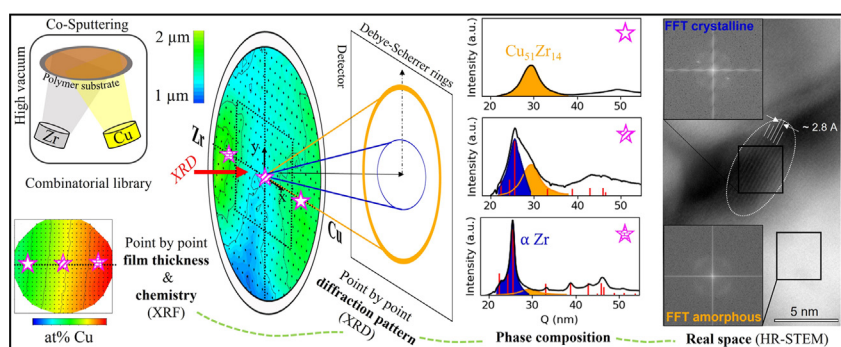
ABSTRACT

We report for the first-time combinatorial synthesis of thin film metallic glass libraries via magnetron co-sputtering at the limit of crystallinity. Special care was taken to prepare extremely pure CuZr films (1–2 µm thickness) with large compositional gradients ($Cu_{18.2}Zr_{81.8}$ to $Cu_{74.8}Zr_{25.2}$) on X-ray transparent polymer substrates in high-vacuum conditions. Combined mapping of atomic structure (synchrotron radiation) and chemical composition (X-ray fluorescence spectroscopy) revealed that over the entire composition range, covering multiple renowned glass formers, two phases are present in the film. Our high-resolution Synchrotron approach identified the two phases as: untextured amorphous $Cu_{51}Zr_{14}$ (cluster size 1.3 nm) and textured, nanocrystalline α-Zr (grain size 1–5 nm). Real space HR-STEM analyses of a representative composition substantiate our XRD results. Determined cluster and grain sizes are below the resolution limit of conventional laboratory-scale X-ray diffractometers. The presented phase mixture is not permitted in the Cu-Zr phase diagram and contrary to existing literature. The phase ratio follows a linear trend with amorphous films on the Cu-rich side and increasing amounts of α-Zr with

---

* Corresponding author at: Department of Materials Science, Montanuniversitaet Leoben, Franz Josef Strasse 18, A-8700, Leoben, Austria.
 E-mail address: barbara.putz@unileoben.ac.at (B. Putz).
[1] Equal contributions.

increasing Zr content. While cluster size and composition of the amorphous phase remain thorough the compositional gradient, crystallite size and texture of the nanocrystalline α-Zr change as a function of Zr content.

1. Introduction:

Metallic glasses (MGs) have attracted considerable research interest over the last decades for their unique mechanical [1] and functional properties [2,3]. Their outstanding property profile predominantly originates from the stable amorphous atomic structure and absence of grain boundaries, facilitated by mixing of elements with different atomic size. Potential candidates are found in the vicinity of deep eutectics in binary or multinary phase diagrams, often assisted by quantum mechanical guidance [4–6], however, the fundamental understanding of glass formation is still incomplete. Thus far, more than 30 elements [2] have been reported as constitutional components in MG-forming alloys.

By virtue of physical vapor deposition (PVD), kinetic limitations in traditional bulk metallic glass formations can be bypassed, resulting, for instance, in so-called ultrastable thin film metallic glasses (TFMG) with extraordinary thermodynamic and kinetic stability and exceptional mechanical properties [7,8]. Even though the composition window for achieving fully amorphous thin films via PVD is much wider than that for bulk processing routes, the thin film form is less exploited. Recently, amorphous TFMGs have been proposed for a number of different engineering fields [3] including flexible and rigid micro-electronics [9,10], biomedical applications [11] and energy storage [12–14]. Moreover, PVD has also been reported as a convenient way to fabricate amorphous-nanocrystalline (nc) composite thin films [15,16], where direct precipitation of a variety of nanoscale structures can further enhance mechanical and functional properties of amorphous matrix [15,17–19]. In such nanocomposites, the volume fractions of amorphous and nanocrystalline (nc) phases vary as a function of chemical composition, from a largely amorphous matrix with finely dispersed nanocrystals (NCs) (Al-16 at.% Mo [17]) to a nc matrix with amorphous phase along grain boundaries (Cu-0.5–8 at.% Zr, [18]). Molecular dynamics (MD) simulations on PVD development of glassy thin films [20] revealed that besides composition, the deposition setup also influences the phase composition: while simultaneous deposition of different elements results in a fully amorphous films, sequential deposition results in a nc composite.

From a variety of PVD methods, magnetron sputtering is used most commonly to fabricate amorphous and nc-composite thin films [15,21], either from multi-element alloy targets or by co-deposition from single elemental targets. The latter approach allows deposition of multinary combinatorial libraries with large composition gradients in a single deposition run [2,22]. To fully exploit the benefits of such libraries, high throughput analyses methods with sufficiently high spatial resolution are required to study, for e.g., glass forming ability [23] and optimize desired mechanical or functional property in a time and resource efficient manner [2,22,24–30]. Particularly relevant for TFMG and nanocomposites is high-resolution (HR) characterization of the atomic arrangement. Suitable methods include transmission electron microscopy (TEM) or X-ray diffraction (XRD). HR-TEM imaging can directly uncover nanocrystalline structures of a few nm [18,31] and, combined with selected electron area diffraction (SEAD), confirm the crystalline (discrete spots) or amorphous (diffraction rings) nature of a specific area. However, the crystal orientation relative to the electron beam, a limited field of view

per sample and laborious TEM sample preparation can influence the detectability of nanocrystals. XRD is an indirect way of determining short or long-range order of materials based on their diffraction signal. Often, the method does not require additional sample preparation steps and large areas can be mapped in a time efficient manner. However, the crystal size detection limit of laboratory diffractometers, developed to characterize crystalline materials above 1 wt% from narrow high intensity peaks, is around 2–2.5 nm [32].

Amorphous materials are lacking long-range crystallographic order and produce broad humps with low intensities in XRD patterns [33]. Their structures are usually expressed in terms of the atomic pair-distribution function (PDF), G(r), describing the probability of finding two atoms separated by the distance, r [34]. PDF can be determined through the Fourier-transformation of the structure factor, S(Q), which can be directly measured by diffraction experiments [34]. The diffraction signal of amorphous-nc composites is a combination of overlapping crystalline and amorphous patterns. Unambiguous structural characterization requires a combination of laboratory XRD with at least HR-TEM or differential scanning calorimetry (DSC), for the above-mentioned experimental limitations. Alternatively, the use of high intensity synchrotron X-ray sources can sufficiently increase the resolution while at the same time significantly decreasing the acquisition time. This allows for time-resolved *in situ* observation of deformation [34] or annealing induced crystallization [35–38] processes in MGs as well as mapping of the phase composition in multinary combinatorial libraries.

The latter is reported in this work, investigating co-sputtered CuZr thin films on XRD transparent polymer substrates over a wide range of chemical compositions ($Cu_{18.2}Zr_{81.8}$ to $Cu_{74.8}Zr_{25.2}$). CuZr alloys have attracted particular research attention for their relative ease of glass formation [5,21,39,40]. Experimentally, the best glass forming compositions have been determined as $Cu_{50}Zr_{50}$ and $Cu_{64}Zr_{36}$ [5] due to the formation of ideally packed icosahedral clusters at the expense of atomic arrangements with excess or deficient free volume [5]. In our study, fully amorphous thin films were only observed for a minority of Cu-rich compositions, contradictory to the beneficial PVD processing conditions and the high glass forming ability of the CuZr system. Owing to the use of synchrotron radiation, the phase composition and atomic structure of individual phases could be identified at the limit of crystallinity, constituting a technologically meaningful step towards time and resource efficient combinatorial development of structural and functional materials and thin films.

2. Experimental

2.1. Thin film deposition

A Mantis QPrep 500 UHV chamber was used to deposit CuZr thin films onto polymer substrates by direct current (DC) magnetron co-sputtering from single element targets. Both targets (Cu and Zr, 99.99% purity, Kurt J. Lesker Company Ltd.) were 7.5 cm in diameter and 2 mm in thickness. The 75 μm thick polyimide (PI) substrates were cleaned with isopropanol and clamped between two Al rings (outer diameter 100 mm) to hold them in

position and to keep them flat, leaving a circle of 90 mm diameter in the center. The substrate mounted in the Al frame is shown in Fig. 1a. Prior to thin film deposition, the substrates were ultrasonically cleaned with acetone and isopropanol (7 min each) and then blown dry with nitrogen. During thin film deposition, the substrate temperature was measured by a thermocouple placed on the backside of the polymer. A thick copper mesh wire was mounted on the backside of the Al ring that connected to a water-cooled surface a few centimeters away to cool the substrates during deposition. As a result, the thermocouple did not detect any temperature change during any of the depositions. The polymer sheets with the Al fixture rings were placed on the sample holder and moved to a position approximately 8 cm below the confocal substrate stage position, towards the magnetrons, as schematically shown in Fig. 1b. This offset enabled a larger compositional gradient on one substrate. Correspondingly, no substrate rotation was applied during deposition.

In total, two depositions were performed, which are referred to as sample 394 and 399 throughout the manuscript. Sputtering was performed at a process pressure of 5×10^{-1} Pa with 15 sccm of Ar flow, and a base pressure of 7×10^{-5} Pa or lower. The specific process parameters for each sample, resulting in a film thickness of ~1–2 μm and a total deposition time of approximately 6 h (deposition rate 2.8–5.6 nm min^{-1}) are summarized in Table 1. Deposition 399 was repeated with a thickness of 50 nm on 3 mm Au grids carrying a carbon support film for analysis by transmission electron microscopy.

2.2. Chemical characterization & thickness measurements

The chemical composition and thickness of each thin film was mapped across the polymer substrates with X-ray fluorescence spectroscopy (XRF, type Fischerscope XRF XDV, accuracy ~0.1 μm). For each sample, more than 400 spots were measured with a beam diameter of 3 mm. XRF maps are shown in Fig. 3. The maximum composition range for each sample was determined as: Cu 39.6–74.7 at.%/Zr 25.2–60.4 at.% and Cu 18.2–52.3 at.%/Zr 47.7–81.8 at.% for samples 394 and 399, respectively.

2.3. Structural characterization with synchrotron radiation and transmission electron microscopy

Structural characterization of the thin films has been performed by X-ray diffraction measurements realized at the high-resolution powder diffraction beamline ID-22 situated in the synchrotron facility ESRF, Grenoble. Diffraction experiments were performed in transmission geometry using a monochromatic beam with a wavelength of 0.2478 Å and a cross-section size of 0.5×0.5 mm^2. The Debye-Scherrer diffraction rings of the coated polymers substrates, placed perpendicularly to the beam, were recorded by a Perkin Elmer XRD 1611CP3 flat panel detector. Samples were scanned step by step along specific directions with a step distance of 2 mm in the horizontal and 4 mm in the vertical direction. The setup is schematically shown in Fig. 2, including the position of the line scan as dotted lines across the sample. Through careful alignment of the polymer substrates at the beamline, the positions of the recorded diffraction patters (Fig. 2, left side) could be matched point by point to the chemical composition obtained via XRF mapping. Instrumental parameters were calculated from the LaB$_6$ powder patterns. Diffraction rings were azimuthally integrated by the Fit2D software [41] and the pair distribution functions were calculated by means of the PDFgetX2 software [42].

The cluster size calculation was determined from the pair distribution function (PFD) signal length, using the cumulative function $CF(x)$ proposed by Bednarčik and co-workers [43], in the following form:

$$CF(x) = \sqrt{\frac{1}{r_{max} - x} \int_{x}^{r_{max}} [G(r)]^2 dr}, \qquad (1)$$

where r_{max} is the maximum value in the reduced pair distribution function, $G(r)$, below the instrument resolution that was fixed to 200 Å. The cumulative function is the decreasing function of the root mean square value in the interval $\langle x, 200 \rangle$, where x is, for the practical calculation, set to $x = 0$. The cluster size is, then, the r-length determined from the point where $CF(x)$ drops to the value below signal noise corresponding to the high-r region.

Texture determinations were carried out using the E-WIMV approach implemented in Rietveld refinement based on the MAUD software [44].

For a selected representative chemical composition, structural characterization was performed by imaging on a probe-corrected Thermo Scientific Titan Themis 200 G3 transmission electron microscope (TEM) operated at 200 keV. Energy dispersive X-ray spectroscopy was acquired with the integrated SuperX detector to confirm the chemical composition and analyzed using the Velox Suite, Thermo Fischer, where the K-lines were employed for the analysis of Cu and Zr concentrations.

3. Results and discussion

3.1. Film thickness and chemical composition

After deposition, the chemical composition and thickness of the CuZr films were mapped across the polymer substrates. The results of this XRF mapping are summarized in Fig. 3. Generally, film thickness values are approximately ranging between 1.4 and 2.3 μm for the two different samples (Fig. 3a and b). The overall thickness difference between 394 and 399 is a result of the different sputter parameters used to enlarge the compositional gradient between the two samples. As a result of co-deposition without substrate rotation, a small thickness gradient was observed on each sample, with slightly increased thicknesses on the Zr-rich side. Additionally, for sample 394 (Fig. 3a), an area of slightly increased film thickness is observed in the upper half of the sample, spanning across the entire compositional range. The thickness variations need to be considered during subsequent analysis and interpretation of the XRD data. From initial calculations based on geometrical considerations (sample-detector distance, wavelength), increasing the film thickness by 1 μm results in an increase in Debye-Scherrer ring radius by less than 0.06 μm. This shift is not measurable with the utilized setup as the pixel size of the used detector is 100×100 μm^2. Therefore, the thickness variations do not affect the comparative XRD analysis and derived conclusions.

The utilized deposition approach resulted in a large and homogeneous composition gradient across the polymer substrates (Fig. 3c–f). As is evident by comparing samples 394 and 399, a slight variation in sputter parameters enabled enlargement of the accessible total compositional gradient. Combining both samples, the total chemical composition ranges from Cu$_{18.2}$Zr$_{81.8}$ (sample 399) to Cu$_{74.8}$Zr$_{25.2}$ (sample 394). It is also evident from Fig. 3c–f that the two samples have a certain overlap in the intermediate composition range.

3.2. Film microstructure

In Fig. 4 all recorded, integrated, and normalized diffraction patterns are shown and summarized for both samples 394 and 399, respectively. In principle, two different phases have been identified within the investigated composition range, as detailed in the following paragraph. Starting with sample 394 (Fig. 4a), the diffrac-
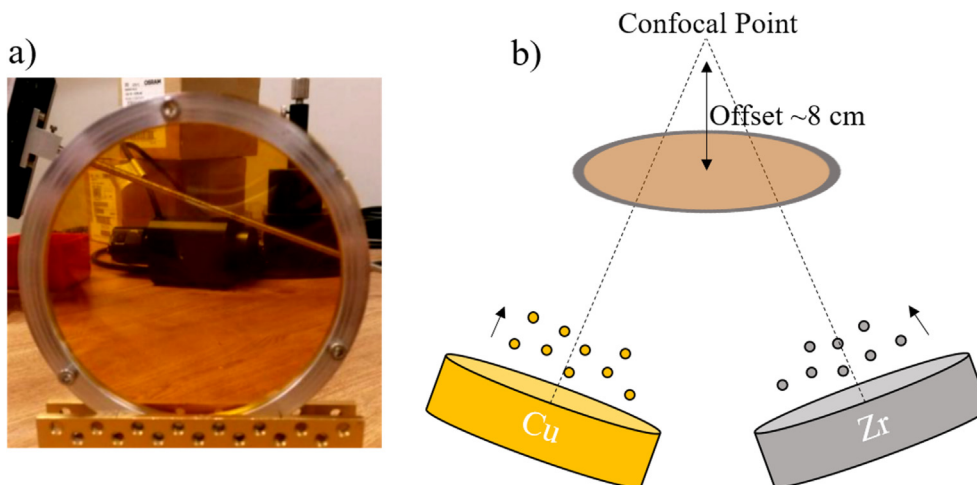
Fig. 1. Co-sputtering of CuZr thin film combinatorial libraries on polymer substrates. (a) Polymer substrate mounted in a frame of two Al rings to keep it flat and enable cooling during deposition. (b) Schematic of the non-confocal sputter geometry, whereby the offset of approximately 8 cm enables a larger compositional gradient on each substrate.

Table 1
Process parameters for thin film deposition.

Sample	Power (W)		Current (mA)		Voltage (V)		Offset from confocal position (cm)
	Cu	Zr	Cu	Zr	Cu	Zr	
394	35	106	85	300	408	356	8
399	13	100	40	300	319	335	8
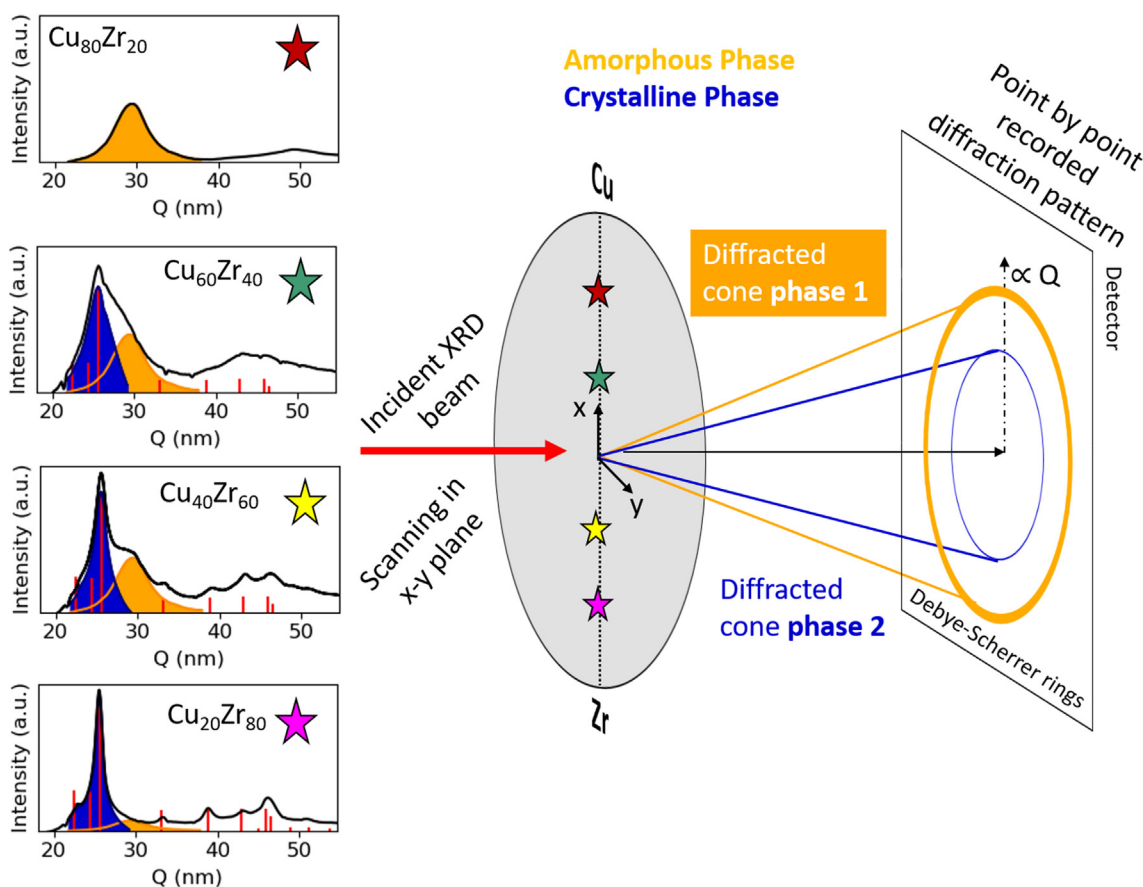
Fig. 2. Schematic of the synchrotron setup (right) and representative diffraction patterns (left) collected point by point along a specific direction on the substrates, corresponding to different chemical composition of the binary CuZr system. Two different phases were identified as a function of chemical composition: amorphous $Cu_{51}Zr_{14}$ (orange peak) and crystalline Zr (blue peak). The red vertical lines indicate the positions of additional Zr Bragg reflections. Experimental schematic modified from Ref. [45].
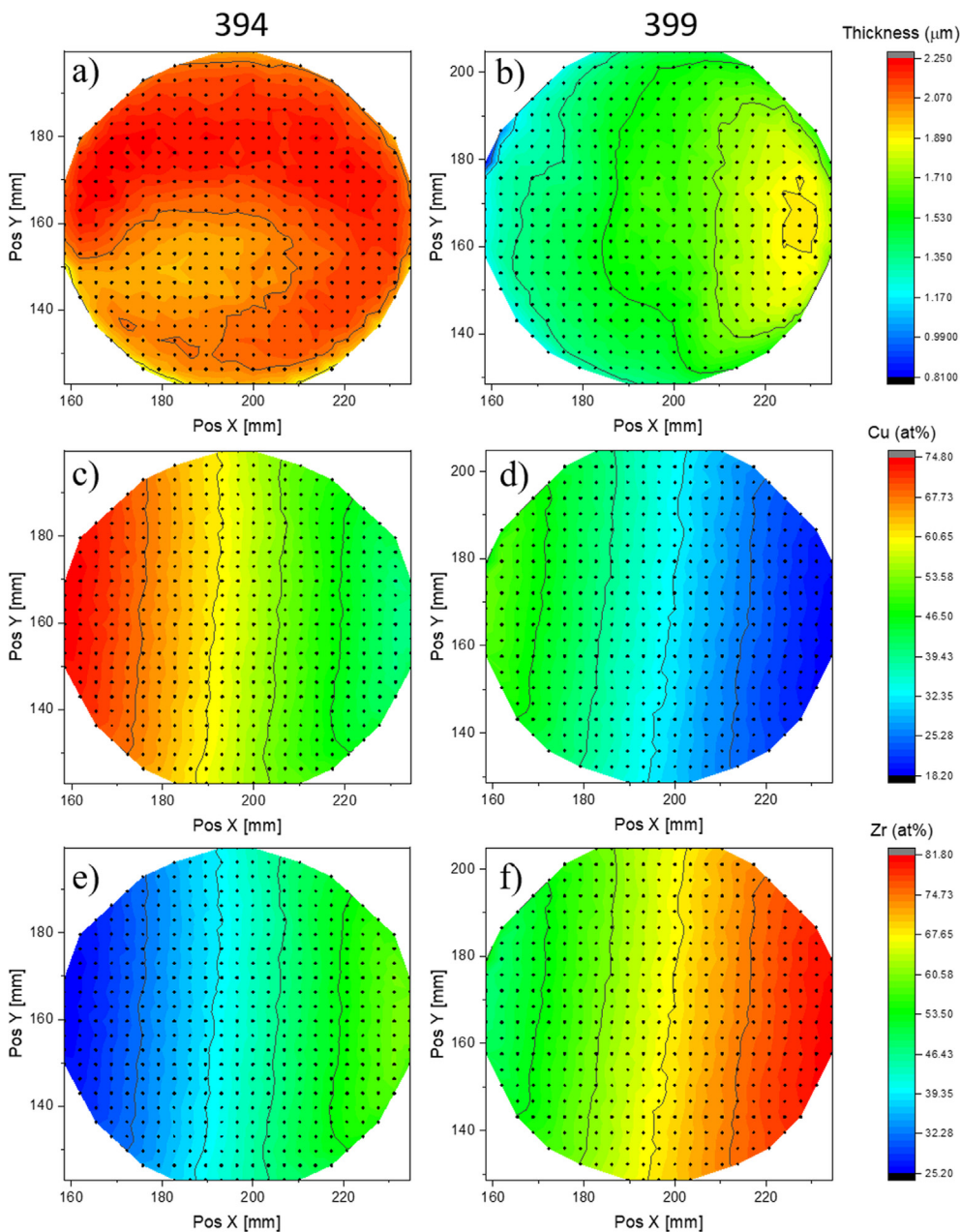
Fig. 3. XRF mapping of film thickness and chemical composition of the CuZr thin films. (a, b) Film thickness of samples 394 and 399, respectively, whereby overall differences stem from a deliberate, slight variation of sputter parameters. (c, d) at.% Cu and (e, f) at.% Zr for samples 394 and 399, respectively. A large and homogeneous composition gradient was achieved by non-confocal, co-sputtering without substrate rotation.
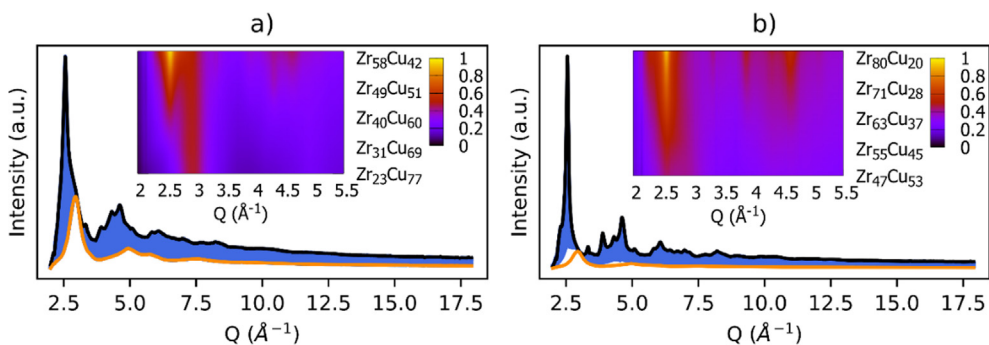
Fig. 4. Diffraction patterns of sample (a) 394 and (b) 399. Inset figures present the evolution of diffraction patterns of CuZr thin films as a function of chemical composition. For sample 394 (a), the two curves obtained from either end of the compositional gradient are shown in orange (Cu rich side) and black (Zr rich side), respectively. The orange diffraction pattern shown in (b) (sample 399) is the first diffraction pattern from sample 394 (Cu rich side) and is included for comparison.

tion pattern obtained from the sample position with the highest Cu content ($Cu_{77}Zr_{23}$) is drawn in orange (phase 1). In contrast, the diffraction pattern from the sample site with the highest Zr content is shown in black. One can see from the inset in Fig. 4a that as the Zr content increases from 23% to 58%, new peaks appear (phase 2) and their intensity increases steadily, while the peak positions remain constant up to the maximum Zr content, which was up to 82% in the sample 399 (Fig. 4b). It should be noted that the wide diffraction signal obtained in places with the highest Cu contents (orange curve, phase 1) is found in all recorded diffraction patterns, for both samples 394 and 399, and only the proportion of the intensity of the two phases changes. The phase whose proportion increases with increasing Zr content (phase 2) was identified as the Zr phase (according to PDF2 database ICDD 5-50665 [46]). The theoretical positions and relative intensities of Zr diffraction peaks are included in Fig. 5 as vertical blue lines, indicating good agreement with the experimentally obtained diffraction patterns at higher Zr contents (Fig. 5d). However, the phase with a high Cu content (orange curve, phase 1) could not be unambiguously determined, because the diffraction signal is very wide, which could, at first glance, indicate an amorphous structure. The peak width of phase 1 (orange peak, Fig. 2) was determined as ~1.1° (0.49 Å^{-1}) and remains constant throughout the investigated composition gradient. In contrast, the peak with of phase 2 (Zr phase, blue peak Fig. 2) varies across the gradient. On the Cu rich side, the peak width of phase 2 ($1.73° = 0.77$ Å^{-1}) is slightly larger than phase 1, corresponding to a smaller crystallite size in Fig. 7, and decreases with increasing at.% Zr ($0.61° = 0.27$ Å^{-1} on Zr rich side).

The highest match of the orange diffraction signal in Fig. 4a, compared to the database was found with the intermetallic $Cu_{51}Zr_{14}$ phase (according to PDF2 database ICDD 42-1185 [47]). Of all reported CuZr intermetallics [21], $Cu_{51}Zr_{14}$ has the most negative formation enthalpy (-25.2 kJ/mol), making it the most stable. The theoretical positions and relative intensities of $Cu_{51}Zr_{14}$ diffraction peaks are shown in Fig. 5 as vertical orange lines, indicating good agreement with the experimentally obtained diffraction patterns at high Cu contents (Fig. 5a). One can see that the diffraction patterns from areas with the same nominal chemical composition (Fig. 5b and c) have slightly different peak shapes. It will be shown in the further evaluation of the data that the greatest impact on a signal broadening of the 399 sample stems from the smaller crystallite size of the Zr phase (Fig. 7a). Rietveld refinement was carried out to determine the crystallite size of the individual phases by using the mentioned phases Zr and $Cu_{51}Zr_{14}$. Two representative refinements are presented in Fig. 6, showing that in both cases, there is good agreement between the measured data (bottom) and the Rietveld fit (top). The results show that over the whole range of investigated chemical compositions, the crystallite size of the $Cu_{51}Zr_{14}$ phase was very similar. In both samples (394 and 399) the evaluated cluster size of $Cu_{51}Zr_{14}$ ranges between 13 and 18 Å (see Fig. 7, grey and dark red lines). On the other hand, the Zr phase shows a clear increase in the crystallite size with increasing Zr content (Fig. 7, black and bright red triangles). In addition, the crystallite size (D) of the Zr phase was calculated using the well-known Scherrer equation:

$$D = \frac{K\lambda}{\beta \cos\theta} \tag{2}$$

where λ is the wavelength of used radiation, β and θ are the integral breadth and the position of the investigated Bragg peak (1 0 1) of the Zr phase, respectively, and K is the shape constant which remained equal to 1. The fitting procedure was carried out on an azimuthal fully integrated diffraction pattern after subtraction of the $Cu_{51}Zr_{14}$ diffraction signal (the first diffraction pattern of sample 394). The results are presented in Fig. 7 and correspond to crystallite size values obtained by Rietveld refinement.

To compare the results obtained by Rietveld refinement and Scherrer calculation, the signal length of the pair distribution function, corresponding to the cluster size of the measured material, was analyzed. In such an analysis, it is not necessary to assume or know the phase composition of the investigated material. Pair distribution functions were calculated using the PDFgetX2 software and then the signal length was determined using the cumulative function CF(r), as described in the experimental section. In the pair distribution function of the highest Cu content (Fig. 7b, top), which has been attributed to the $Cu_{51}Zr_{14}$ phase, five coordination shells are visible with a signal length, δ, close to 13 Å. The cluster size is constant with increasing Zr content up to 40%, then, the signal length, equal to the cluster size, starts to increase (see Fig. 7, black and red circles). There is good agreement in the calculated cluster sizes for the overlapping composition ranges of sample 394 and 399 (~57–62% Zr). It is also worth noting that the results of the cluster/crystallite sizes of the two independent evaluation approaches (Rietveld vs. PDF) are in good agreement for both samples with a difference of approximately less than 0.3 nm.

The fractions of individual phases in the thin films ($Cu_{51}Zr_{14}$ vs. Zr) as a function of the chemical composition is shown in Fig. 8. The different analysis approaches summarized in Fig. 5 yield good agreement in terms of phase ratios. Due to weak signal, it was not possible to perform Rietveld refinement in places with a very small proportion and diffractive volume of the Zr phase. Therefore, the phase ratio was first determined from the peak areas belonging to the individual phases, as shown in the insets of Fig. 8 (orange peak: $Cu_{51}Zr_{14}$; blue peak: Zr). The integration boundaries of the areas were set constant for all diffraction patterns. As the Zr content in the sample increases, the proportion of the Zr phase (blue peak) increases. A similar dependence was also found by using Rietveld refinement. Following these observations, a simple theoretical calculation of the Zr phase ratio dependence on the chemical composition is also included in Fig. 8. Based on the chemical composition of the thin film on the Cu-rich side ($Cu_{77}Zr_{23}$), it was assumed that all the Cu was consumed to form the $Cu_{51}Zr_{14}$ phase. It is thereby important to note that the chemical composition of $Cu_{77}Zr_{23}$ corresponds almost exactly to the elemental ratio of $Cu_{51}Zr_{14}$. If all Cu atoms form the $Cu_{51}Zr_{14}$ phase with Zr, then the rest of the Zr atoms form the observed crystalline Zr phase. The theoretical phase ratio calculation following this theory was carried out based on the molar weight of the elements and their atomic ratios in each phase. Surprisingly, this first principle calculation (Fig. 8, blue circles) is very close to the results obtained from the measured data.

The diffraction results clearly show that only two phases are present in the whole composition range of the combinatorial CuZr thin films, namely the $Cu_{51}Zr_{14}$ phase and the pure Zr phase. In both cases, peak positions remain constant throughout the investigated composition range and only relative intensity changes between $Cu_{51}Zr_{14}$ and Zr peaks are observed. Correspondingly, the phase ratio depends on the compositional gradient, whereby in the Cu rich region, almost exclusively, the $Cu_{51}Zr_{14}$ phase is present and in the Zr rich region the Zr phase prevails with up to 80%. In the case of the Zr phase, it can be stated that it has a very fine, nanocrystalline microstructure, whereby the crystallite size increases with increasing Zr content (from ~1 to 5 nm). Even in regions where the crystallite size of this Zr phase is below 10 Å (<30% Zr, Fig. 7), a preferred crystallographic orientation is unambiguous in the diffraction pattern. This preferred orientation of Zr was found to be very similar throughout the compositional range and is documented by the inverse pole figures in Fig. 9. In the case of the $Cu_{51}Zr_{14}$ phase, it is permissible to call it amorphous. Firstly, amorphous materials have a defined short-distance ordering. Comparing our results to published data examining CuZr binary metallic glasses [48–50], both the number of coordination envelopes
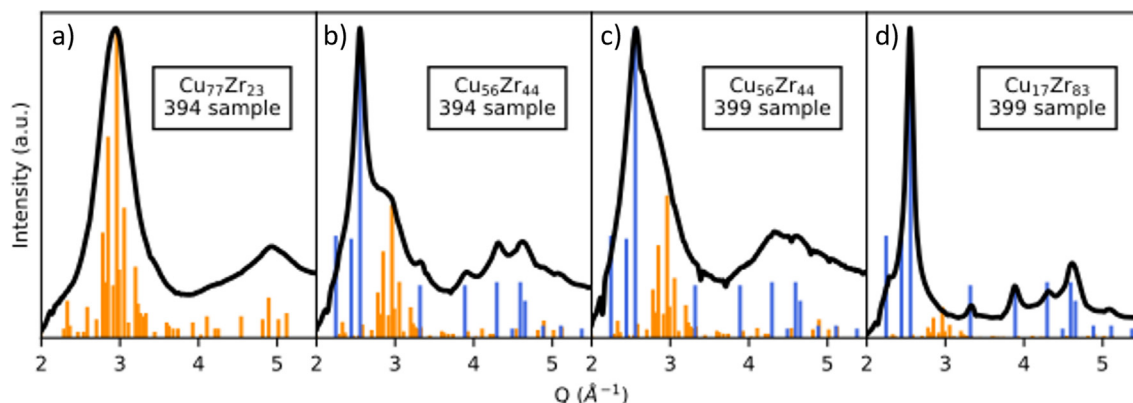
Fig. 5. Diffraction patterns of CuZr thin films as a function of chemical composition, with the Zr (blue) and $Cu_{51}Zr_{14}$ (orange) phase peak positions from PDF2 database.

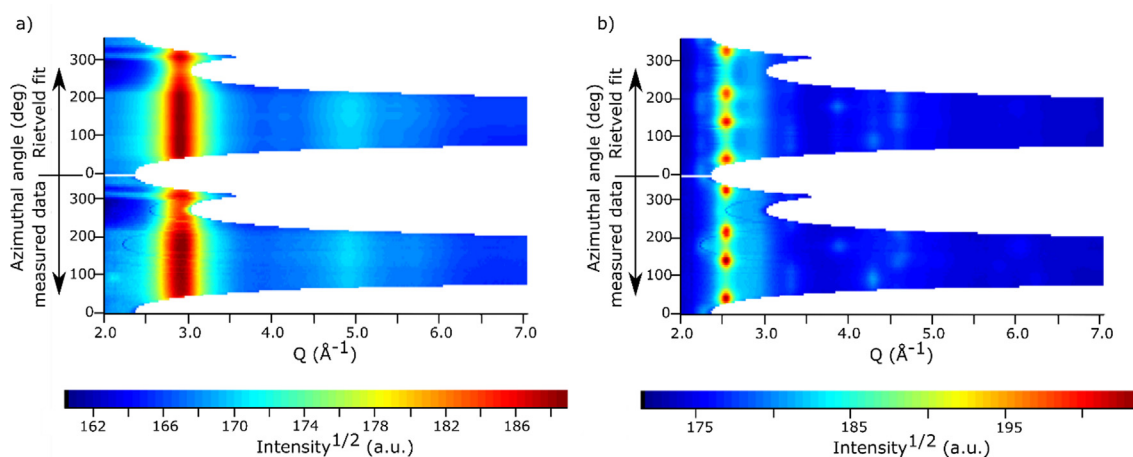**Fig. 6.** Rietveld refinement of the diffraction pattern for (a) $Cu_{77}Zr_{23}$ and (b) $Cu_{56}Zr_{44}$ measured on sample 394. There is good agreement between the measured data and the Rietveld fit.
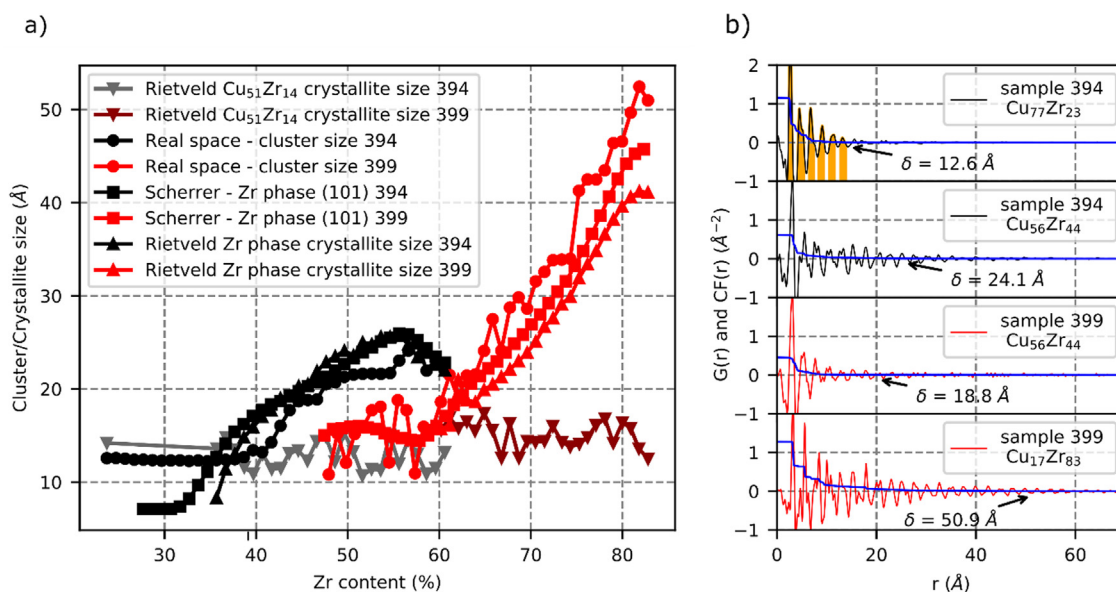

Fig. 7. (a) Crystallite/cluster size based on Rietveld refinement, Scherrer calculation and pair distribution function (PDF) and as a function of chemical composition. Results indicate good agreement between the two samples and the three independent analysis methods. (b) Pair distribution function (PFD, G(r), black & red curves), cumulative function CF(r) (blue curves) and signal length, δ, of CuZr thin films as a function of chemical composition.
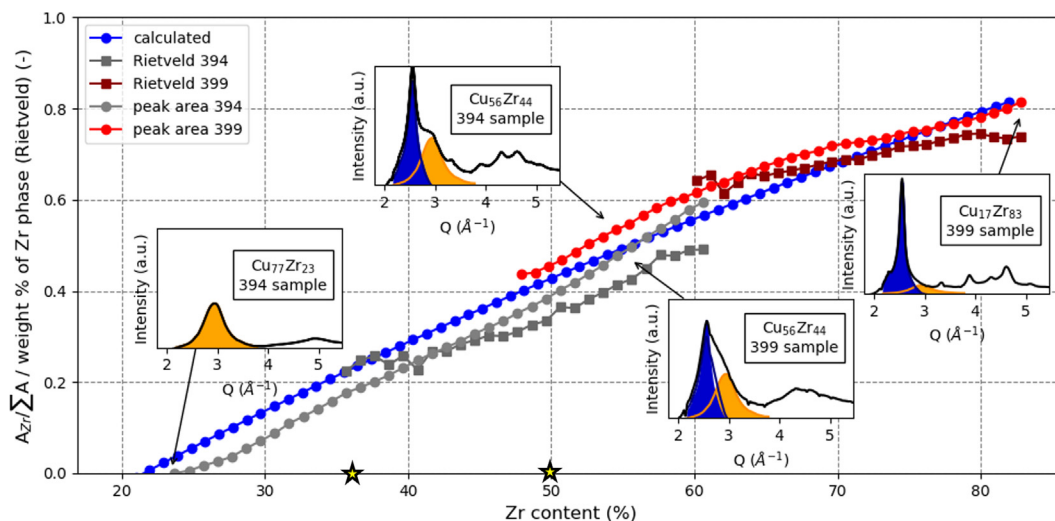
Fig. 8. Phase ratio dependence on chemical composition of combinatorial CuZr thin films. The ratio of the $Cu_{51}Zr_{14}$ and Zr phase, obtained from relative peak areas, Rietveld refinement and theoretical calculations are in good agreement. Yellow stars mark typical glass forming compositions.
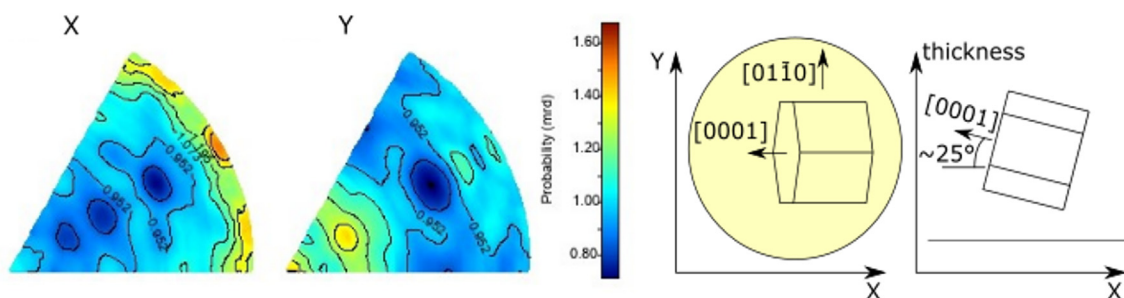

Fig. 9. Representative inverse pole figures of the Zr phase show the preferred crystallographic orientation. X and Y direction correspond to substrate coordinate system (according to Fig. 3). Schematic on the right side schematically shows the preferred orientation of the hexagonal close packed structure on the substrate.

(five, highlighted in orange in Fig. 7b, top image) and the signal range (13 Å) suggest that it could be an amorphous type of phase. Furthermore, the Debye-Scherrer rings in the diffraction pattern are smooth without any high-intensity spots. Considering the constant cluster size ($\sim$13 Å), independent of the varying $Cu_{51}Zr_{14}$ content over the compositional gradient, combined with the observed crystallographic isotropy, this $Cu_{51}Zr_{14}$ phase can be classified as amorphous. The cluster size of 1.3 nm is at the limit of what has been observed for nanocrystalline materials. Amorphization of intermetallics occurs below 1.7–12 nm grain size, depending on the material and the grain boundary structure related to the preparation technique [51,52]. Considering the crystal structure of $Cu_{51}Zr_{14}$, the measured cluster size is roughly the same as the dimensions of the unit cell (a = b = 11.25 Å, c = 8.275 Å [53]; atomic radius Zr: 0.160 nm, Cu: 0.128 nm [21]).

High resolution scanning TEM imaging (HR-STEM) was performed on selected chemical compositions to substantiate our interpretation of the XRD results. Since sample requirements for HR-STEM strongly differ from Synchrotron-XRD, depositions were repeated under identical process conditions but limiting the total film thickness to 50 nm (electron transparent). This way, HR-STEM data can be recorded through the thickness on pristine films, avoiding ion beam induced damage, contamination or changes to the microstructure (e.g. crystallization) during conventional or focused ion beam lift-out sample preparation. Fig. 10a shows a top-view HR-STEM image of $Cu_{47}Zr_{53}$ deposited using the conditions of sample 399; the composition was determined by STEM-EDX analysis, Fig. 10b. We are resolving the C and O from the

EDX spectra but are excluding it from the composition measurement as it constitutes the carbon support film and any minor natural oxide formation upon transfer between deposition chamber and TEM. In HR-STEM, both crystalline and amorphous regions are clearly visible, as confirmed by the local fast Fourier transform (FFT) insets. The crystalline regions were identified where the film thickness was lowest, and the high angle annular dark field (HAADF) contrast is therefore darkest. Such locations helped minimize the volume of amorphous phase above or below the crystallites, to enable adequate resolution of crystallinity. The lattice plane spacing of the crystalline regions ($\sim$2.8 Å, averaged across 10 consecutive planes) is consistent with the $\{1\bar{1}00\}$ planes of hexagonal α-Zr. The size of the crystalline regions measured from HR-STEM images is $\sim$5 nm, and therefore slightly larger than that determined from XRD for this composition (1.5–2.5 nm, Fig. 7a). In fact, the crystals are non-spherical: their elongated ellipse shape (3.5 × 6.6 nm in the centered example in Fig. 10a, outlined with dashed white lines) could contribute to the observed grain size difference. Typically, the coherent domain size as determined by XRD is smaller than the grain size determined from optical or electron imaging [54]. Despite the spatially resolved EDX analysis (Fig. 10b), we cannot draw any clear conclusion about a difference in composition of the two phases as we always probe differing proportions of both phases in the volume through the thickness of the thin film TEM sample. Instead, the average composition is superimposed by horizontal dashed lines.
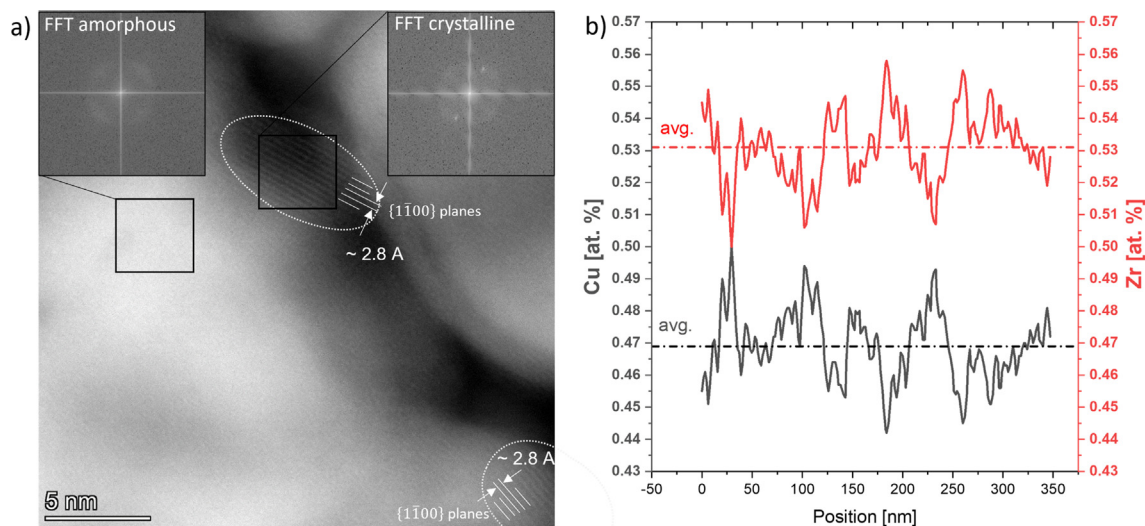
Fig. 10. (a) Top-view HR-STEM-HAADF image of 50 nm $Cu_{47}Zr_{53}$ showing that both amorphous and crystalline regions are present in the thin film, as confirmed by local FFT (insets top left and right, respectively). Nanocrystals are outlined with white dashed lines. Lattice planes are indicated by continuous white lines. (b) Spatially resolved STEM-EDX line scan showing the Zr and Cu composition of a generic area, with superimposed dashed lines indicating the average composition.

In general, Cu–Zr alloys are known for their relative ease of glass formation, with a wide glass-forming composition range [5,39,40]. Experimental observations (high energy X-ray diffraction, neutron diffraction and extended X-ray absorption spectroscopy) [48,55,56] on rapidly quenched CuZr compositions and simulation results (combined molecular dynamics simulations and first-principles approach) [5] agree on the best glass forming compositions for rapid solidification processes being located at $Cu_{50}Zr_{50}$ and $Cu_{64}Zr_{36}$, due to the formation of ideally packed icosahedral clusters [5]. Both of those compositions are within the range investigated in this study ($Cu_{18.2}Zr_{81.8}$ to $Cu_{74.8}Zr_{25.2}$; yellow stars in Fig. 8)), however, no fully amorphous film has been observed at either location. Rather, both compositions perfectly follow the linear trend of phase ratio dependence between the amorphous $Cu_{51}Zr_{14}$ and crystalline Zr phase, as visible in Fig. 8. Also, the potential composition of the amorphous phase ($Cu_{51}Zr_{14}$) is far from the ideal glass formers. Previously, CuZr thin films have been reported to show a broad composition range of amorphous regions without any preferential glass forming regions around Cu_{50} and Cu_{64}. Most of these studies [21,57–59] have used x-ray diffraction to come to this conclusion. In our study, we never observed fully amorphous films. Almost single-phased amorphous films (Cu_{51}-Zr_{14}) with extremely faint, unquantifiable traces of α-Zr are found at high Cu concentrations (70–75% Cu). Around 35% Zr and above, the α-Zr peaks become very distinctive. For magnetron sputtered Cu-rich CuZr thin films, Zhang et al. [18] reported a matrix of nanocrystalline (nc) Cu grains, whereby additions above 0.5 at.% Zr yielded the formation of an amorphous phase at the grain boundaries, as shown by laboratory XRD and TEM analysis. With additions of 8 at.% Zr, a continuous amorphous layer with a thickness of 3 ± 1 nm surrounded the nc-Cu grains, whereby the chemical composition of this amorphous phase is not further specified. Unfortunately, the highest Zr content reported in Ref. [18] (Cu_{92}-Zr_8) is outside the composition range of our study, where no indication of nc Cu was observed at the Cu rich end ($Cu_{74.8}Zr_{25.2}$). While the initial deposition conditions in Ref. [18] are comparable to ours, an additional annealing treatment (250 °C–2 h) could contribute to the observed differences. Alternatively, increasing Zr addition in Ref. [18] could further the growth of the amorphous grain boundary layer, progressively eliminating the nc Cu grains. In a separate study on a Cu-rich co-sputtered Cu-Zr thin film

library (2.1 μm thickness, Zr 2.5–6.5 at.%), Oellers et al. [28] report fcc Cu Bragg peaks for all Zr contents, whereby a gradual shift of all Cu reflections with increasing Zr content indicates the formation of a solid solution. Complementary TEM diffraction shows reflexes of a pure Cu phase, no reflexes of pure Zr and a negligible amount of Cu_5Zr phase.

Besides Cu-rich cases, Apreutesei et al. [21] obtain glassy CuZr films via PVD co-sputtering over a wide composition range. Within 33.3–89.1 at.% Cu (20–77 at.% investigated in our study), fully amorphous films without any crystalline diffraction peaks are observed, which even maintain their amorphous structure during post annealing at temperatures higher than 277 °C. TEM analysis of our films clearly show co-existent amorphous and nanocrystalline regions in $Cu_{47}Zr_{53}$. Outside this fully amorphous regime presented in [21], clearly crystalline and textured fcc (1 1 1) Zr and Cu films are obtained, respectively. On the Zr-rich side (75–71.5 at.% Zr), traces of fcc-Zr phase are found in the XRD signal, embedded into the broad amorphous hump. Intermetallic phases, including $Cu_{51}Zr_{14}$, evolve with temperature and Cu contents in a multistage crystallization process, whereby the $Cu_{51}Zr_{14}$ phase only develops in films with more than 45 at.% Cu content.

Fundamentally, the microstructure of vapor deposited thin films depends on the mobility of atoms arriving at the surface. There is a general consensus that the substrate temperature (T_{sub}) during deposition is a critical variable, with the optimal T_{sub} for creating ultrastable glasses near the glass transition temperature, T_g. While a raised substrate temperature undoubtedly enhances the surface mobility, ordinary and ultrastable TFMG ($Zr_{46}Cu_{46}Al_8$) have also been synthesized on cold substrates (RT) with an inverse dependence of T_g on the deposition rate (range 1–10 nm min^{-1} [7]), supporting the idea of an enhanced surface mobility mechanism. The characteristic time of surface dynamics associated with finding ultrastable configurations was identified as ~17 s [7]. The deposition rate utilized in this work (2.8–5.6 nm min^{-1}) is well within the range reported for glassy microstructures. Based on the atomic radius of Zr (0.160 nm) and Cu (0.128 nm), the thickness of the surface monolayer (ML) is estimated to be ≈0.288 nm. At a deposition rate of 5.6 nm min^{-1}, the minimum surface residence time for atoms to freely explore stable configurations before being buried can be estimated as ≈3 s. Further estimation of surface mobility is exacerbated by the fact that in

multicomponent systems, likely each element moves with a different timescale [60], and strongly dependent on the type of surface.

A second important influencing factor for glass formation during vapor deposition is the base pressure and related impurity concentrations. Compared to extremely pure bulk MGs, the impurity levels (e.g. O_2) during PVD can reach levels of 100 ppm (10^{-7} Pa) to 1% (10^{-5} Pa). While O_2 as an impurity is known to aid glass formation and stability even at low concentration, accurate detection in the ppm regime remains extremely challenging, for example using glow discharge optical [61–63] emission spectrometry (GDOES). The high vacuum (HV) conditions and cleanliness of our chamber could contribute to the fact that we do not observe glass formation at typical glass forming compositions.

Combined MD and experimental results on Cu–Zr thin films [20] indicate that the deposition geometry also influences surface diffusion of arriving species and resulting microstructure: Simultaneous deposition of Cu and Zr atoms using both pulsed laser deposition and magnetron sputtering yields amorphous CuZr thin films ($Cu_{30}Zr_{70}$, $Zr_{60}Cu_{40}$), due to the formation of icosahedral (ICO)-like clusters that impede nucleation. However, sequential deposition of Cu and Zr atoms from a sectored target results in the formation of a nanocrystalline composite (nanograins of Zr_2Cu and α-Zr, embedded in an amorphous matrix, no trace of Cu grains).

Regarding atom energies, impurity levels and sputter geometry, our process is similar to the conditions found in literature. Besides deposition parameters, also the substrate can influence the resulting thin film microstructure, due to different growth or cooling conditions. Most studies on TFMG utilize rigid Si substrates (thermal conductivity at RT 156 Wm^{-1} K^{-1} [64]), e.g. electrically floating to minimize ion–solid interactions at the growing film surface [20]. Our polymer substrates (thermal conductivity at RT $\sim$ 0.2 Wm^{-1} K^{-1} [65]), were cooled during deposition to facilitate glass formation and kept on ground, depleting all incoming charge from the thin film during deposition. Therefore, the Al fixation rings, holding initially nonconductive PI substrates, were grounded through the substrate holder stage. As soon as the first continuous monolayer deposit formed on PI, contact was made with the Al rings and the substrate surface became conductive. Differences between generally used Si and our PI substrates can be one potential source of the observed differences in film growth. Contrary to expectations, we did not observe fully amorphous films at any of the typical glass forming compositions, all within our compositional gradient (Fig. 8). Despite simultaneous co-deposition, we clearly observe the formation of nanocrystalline, textured, hexagonal α-Zr above 35 at.% Zr. The fact that increasing amounts of α-Zr are observed with increasing Zr content is somewhat comparable to MD simulations of sequential deposition [20], indicating that crystalline features are more pronounced in the Zr rich areas (Cu_{20}-Zr_{80}). This is explained by interdiffusion of Cu into Zr layers being insufficient to completely consume the Zr layer. A similar diffusion mechanics could be responsible for the formation of nc α-Zr in our case.

Another conceivable scenario could be the deposition of crystalline Zr particles/droplets from the Zr target during sputtering. The particle concentration would then be mainly a function of the distance to the target. The excellent correlation of the linear phase ratio between sample 394 and 399 (Fig. 8) contradicts this theory, since identical chemical composition (overlap of 394 and 399) correspond to different lateral locations and therefore different distances to the Zr target on each polymer substrate (Fig. 3c and d). The fact that the composition of the amorphous phase remains constant throughout the entire composition range under investigation (no peak shift in the XRD signal, orange curves Figs. 4 and 5) further contradicts the particle theory.

A good match was observed between the experimentally measured diffraction pattern of the amorphous phase and intermetallic $Cu_{51}Zr_{14}$ (Fig. 5a). Formation of the $Cu_{51}Zr_{14}$ is not surprising considering that thermodynamically it has the most negative formation enthalpy (-25.2 kJ/mol) of all standardly reported CuZr intermetallics [21], making it the most stable. In the CuZr system, the formation enthalpy of intermetallic phases (ΔH^{inter}) is generally more negative compared to the amorphous state (ΔH^{amor}) over a large composition range (30–65 at.% Zr [66]). Theoretically, the resistance of glass formation against crystallization can be expressed by the γ^* ($\Delta H^{amor}/(\Delta H^{inter}-\Delta H^{amor})$) [67] or γ^{FP} parameter [66], yielding distinctive peaks at known glass forming compositions. In the Cu-Zr phase diagram, this intermetallic is located at $\sim$21.5 at.% Zr [68]; at room temperature, at least one intermetallic phase is separating $Cu_{51}Zr_{14}$ and α-Zr, namely $CuZr_2$ at $\sim$67 at.% Zr. At slightly elevated temperatures, $Cu_{10}Zr_7$ occurs at $\sim$41 at.% Zr. Our synchrotron XRD data indicates no traces of any other intermetallic phase besides $Cu_{51}Zr_{14}$. Clearly, the dual-phase thin films produced by magnetron sputtering do not follow thermodynamic equilibrium predictions and could not be produced by conventional methods, hence constituting a unique and versatile way of fabricating nanocomposite materials. Further research efforts should concentrate on combinatorial characterization of functional and mechanical properties to direct microstructure development (e.g. adjustment of crystallite size and phase ratio) towards application-specific global optima though adjustment of the sputter parameters, electrical substrate biasing or annealing treatments during or after deposition.

4. Summary and conclusions

Combinatorial libraries of binary CuZr thin films were sputtered onto XRD transparent polymer substrates for high throughput mapping of their phase composition over a wide range of chemical composition with synchrotron X-ray diffraction. Thanks to this new high-resolution characterization approach we were able to detect, identify and quantify nm-size clusters in the microstructure that are unheard-of in available literature on PVD Cu-Zr thin films. Contrary to expectations, the following two phases are present throughout the entire composition range under investigation (Zr_{23}-Cu_{77}–Zr_{81}-Cu_{19}): (i) an untextured, amorphous $Cu_{51}Zr_{14}$ phase (cluster size constant: 1.3 nm) and (ii) a nanocrystalline, textured pure Zr phase (grain size 1–5 nm, increasing with Zr content). The presence of amorphous and nanocrystalline phases has been confirmed by HR-STEM imaging of a selected composition. Their relative phase ratio varies linearly across the compositional gradient, whereby at high Cu concentrations, predominantly the Cu_{51}-Zr_{14} phase is present. With increasing amount of Zr, the amount of pure Zr phase increases until it constitutes approximately 80% at the highest Zr concentration. This trend can be explained by the theory of all Cu atoms being used to form the $Cu_{51}Zr_{14}$ phase, and excess Zr atoms forming the nanocrystalline Zr phase. Considering the phase diagram of Cu-Zr, the phase composition presented in this work could not be produced by any conventional fabrication method. Thus far, comparable clusters have only been obtained via thermal treatments introducing a multistage crystallization process. Combinatorial sputter deposition combined with high-resolution mapping of atomic order/disorder could provide an alternative route for growing nanocomposite films with tailored properties, allowing to identify microstructures as a function of deposition parameters and optimize resulting properties in a time and resource efficient manner. Furthermore, the presented combination of high-brilliance XRD and real space HR-STEM data can

help clarify the blurred frontier between nanocrystalline-amorphous, which currently strongly depends on the characterization tool used.

Declaration of Competing Interest

The authors declare that they have no known competing financial interests or personal relationships that could have appeared to influence the work reported in this paper.

Acknowledgements

Data Availability

The raw data required to reproduce the findings of this work cannot be shared at this time as the data also forms part of an ongoing study.

References

[1] M. Ghidelli, H. Idrissi, S. Gravier, J.J. Blandin, J.P. Raskin, D. Schryvers, T. Pardoen, Homogeneous flow and size dependent mechanical behavior in highly ductile Zr65Ni35 metallic glass films, Acta Mater. 131 (2017) 246–259, https://doi.org/10.1016/j.actamat.2017.03.072.

[2] S. Ding, Y. Liu, Y. Li, Z. Liu, S. Sohn, F.J. Walker, J. Schroers, Combinatorial development of bulk metallic glasses, Nat. Mater. 13 (2014) 494–500, https://doi.org/10.1038/nmat3939.

[3] J.P. Chu, J.C. Huang, J.S.C. Jang, Y.C. Wang, P.K. Liaw, Thin film metallic glasses: preparations, properties, and applications, Jom. 62 (2010) 19–24, https://doi.org/10.1007/s11837-010-0053-3.

[4] S. Evertz, I. Kirchlechner, R. Soler, C. Kirchlechner, P. Kontis, J. Bednarcik, B. Gault, G. Dehm, D. Raabe, J.M. Schneider, Electronic structure based design of thin film metallic glasses with superior fracture toughness, Mater. Des. 186 (2020) 108327, https://doi.org/10.1016/j.matdes.2019.108327.

[5] D. Wang, S.J. Zhao, L.M. Liu, Theoretical study on the composition location of the best glass formers in Cu-Zr amorphous alloys, J. Phys. Chem. A. 119 (2015) 806–814, https://doi.org/10.1021/jp5120064.

[6] L. Ward, D. Miracle, W. Windl, O.N. Senkov, K. Flores, Structural evolution and kinetics in Cu-Zr metallic liquids from molecular dynamics simulations, Phys. Rev. B - Condens. Matter Mater. Phys. 88 (2013) 1–10, https://doi.org/10.1103/PhysRevB.88.134205.

[7] P. Luo, C.R. Cao, F. Zhu, Y.M. Lv, Y.H. Liu, P. Wen, H.Y. Bai, G. Vaughan, M. Di Michiel, B. Ruta, W.H. Wang, Ultrastable metallic glasses formed on cold substrates, Nat. Commun. 9 (2018), https://doi.org/10.1038/s41467-018-03656-4.

[8] P. Luo, F. Zhu, Y.M. Lv, Z. Lu, L.Q. Shen, R. Zhao, Y.T. Sun, G.B.M. Vaughan, M. Di Michiel, B. Ruta, H.Y. Bai, W.H. Wang, Microscopic structural evolution during ultrastable metallic glass formation, ACS Appl. Mater. Interfaces. 13 (2021) 40098–40105, https://doi.org/10.1021/acsami.1c10716.

[9] Y. Liu, S. Hata, K. Wada, A. Shimokohbe, Thin film metallic glasses: fabrication and property test, in: IEEE, 14th IEEE Int. Conf. Mirco Electro Mech. Syst., 2001.

[10] O. Glushko, M. Mühlbacher, C. Gammer, M.J. Cordill, C. Mitterer, J. Eckert, Exceptional fracture resistance of ultrathin metallic glass films due to an intrinsic size effect, Sci. Rep. 9 (2019) 1–9, https://doi.org/10.1038/s41598-019-44384-z.

[11] J.P. Chu, J.S.C. Jang, J.C. Huang, H.S. Chou, Y. Yang, J.C. Ye, Y.C. Wang, J.W. Lee, F. X. Liu, P.K. Liaw, Y.C. Chen, C.M. Lee, C.L. Li, C. Rullyani, Thin film metallic glasses: unique properties and potential applications, Thin Solid Films. 520 (2012) 5097–5122, https://doi.org/10.1016/j.tsf.2012.03.092.

[12] B. Sarac, T. Karazehir, M. Mu, B. Kaynak, C. Gammer, T. Scho, A.S. Sarac, J. Eckert, Electrosorption of Hydrogen in Pd-Based Metallic Glass Nano fi lms, 2018. <https://doi.org/10.1021/acsaem.8b00330>.

[13] B. Sarac, Y.P. Ivanov, T. Karazehir, B. Putz, A.L. Greer, A.S. Sarac, J. Eckert, Metallic-glass films with nanostructured periodic density fluctuations supported on Si/SiO2 as efficient hydrogen sorber, Chem. – A Eur. J. (2020), https://doi.org/10.1002/chem.202001596.

[14] B. Sarac, Y.P. Ivanov, M. Micusik, T. Karazehir, B. Putz, S. Dancette, M. Omastova, A.L. Greer, A.S. Sarac, J. Eckert, Enhancement of interfacial hydrogen interactions with nanoporous gold-containing metallic glass, ACS Appl. Mater. Interfaces. 13 (2021) 42613–42623, https://doi.org/10.1021/acsami.1c08560.

[15] F.C. Li, T. Liu, J.Y. Zhang, S. Shuang, Q. Wang, A.D. Wang, J.G. Wang, Y. Yang, Amorphous–nanocrystalline alloys: fabrication, properties, and applications, Mater. Today Adv. 4 (2019) 100027, https://doi.org/10.1016/j.mtadv.2019.100027.

[16] M. Ghidelli, A. Orekhov, A.L. Bassi, G. Terraneo, P. Djemia, G. Abadias, M. Nord, A. Béché, N. Gauquelin, J. Verbeeck, J.P. Raskin, D. Schryvers, T. Pardoen, H. Idrissi, Novel class of nanostructured metallic glass films with superior and tunable mechanical properties, Acta Mater. 213 (2021) 116955, https://doi.org/10.1016/j.actamat.2021.116955.

[17] C. Ophus, E.J. Luber, M. Edelen, Z. Lee, L.M. Fischer, S. Evoy, D. Lewis, U. Dahmen, V. Radmilovic, D. Mitlin, Nanocrystalline-amorphous transitions in Al-Mo thin films: bulk and surface evolution, Acta Mater. 57 (2009) 4296–4303, https://doi.org/10.1016/j.actamat.2009.05.029.

[18] P. Zhang, J.Y. Zhang, J. Li, G. Liu, K. Wu, Y.Q. Wang, J. Sun, Microstructural evolution, mechanical properties and deformation mechanisms of nanocrystalline Cu thin films alloyed with Zr, Acta Mater. 76 (2014) 221–237, https://doi.org/10.1016/j.actamat.2014.04.041.

[19] G. Wu, K.C. Chan, L. Zhu, L. Sun, J. Lu, Dual-phase nanostructuring as a route to high-strength magnesium alloys, Nature 545 (2017) 80–83, https://doi.org/10.1038/nature21691.

[20] G.A. Almyras, G.M. Matenoglou, P.h. Komninou, C. Kosmidis, P. Patsalas, G.A. Evangelakis, On the deposition mechanisms and the formation of glassy Cu-Zr thin films, J. Appl. Phys. 107 (8) (2010) 084313.

[21] M. Apreutesei, P. Steyer, A. Billard, L. Joly-Pottuz, C. Esnouf, Zr-Cu thin film metallic glasses: an assessment of the thermal stability and phases' transformation mechanisms, J. Alloys Compd. 619 (2015) 284–292, https://doi.org/10.1016/j.jallcom.2014.08.253.

[22] M.X. Li, S.F. Zhao, Z. Lu, A. Hirata, P. Wen, H.Y. Bai, M.W. Chen, J. Schroers, Y.H. Liu, W.H. Wang, High-temperature bulk metallic glasses developed by combinatorial methods, Nature 569 (2019) 99–103, https://doi.org/10.1038/s41586-019-1145-z.

[23] N. Liu, T. Ma, C. Liao, G. Liu, R.M.O. Mota, J. Liu, S. Sohn, S. Kube, S. Zhao, J.P. Singer, J. Schroers, Combinatorial measurement of critical cooling rates in aluminum-base metallic glass forming alloys, Sci. Rep. 11 (2021) 1–9, https://doi.org/10.1038/s41598-021-83384-w.

[24] R. Schoeppner, C. Ferguson, L. Pethö, C. Guerra-nuñez, A.A. Taylor, M. Polyakov, B. Putz, J. Breguet, I. Utke, J. Michler, Interfacial adhesion of alumina thin films over the full compositional range of ternary fcc alloy films : a combinatorial nanoindentation study, Mater. Des. 193 (2020) 108802, https://doi.org/10.1016/j.matdes.2020.108802.

[25] R.L. Schoeppner, B. Putz, A.A. Taylor, L. Pethö, K. Thomas, O. Antonin, T. Nelis, J. Michler, Combinatorial materials design approach to investigate adhesion layer chemistry for optimal interfacial adhesion strength, Crystals. 11 (4) (2021) 357.

[26] J. Liu, Y. Liu, P. Gong, Y. Li, K.M. Moore, E. Scanley, F. Walker, C.C. Broadbridge, J. Schroers, Combinatorial exploration of color in gold-based alloys, Gold Bull. 48 (2015) 111–118, https://doi.org/10.1007/s13404-015-0167-z.

[27] X. Xiang, Combinatorial material synthesis and screening: an integrated materials chip approach to discovery and optimization of functional materials, Annu. Rev. Mater. Sci. 29 (1999) 149–171.

[28] T. Oellers, R. Raghavan, J. Chakraborty, C. Kirchlechner, A. Kostka, C.H. Liebscher, G. Dehm, A. Ludwig, Microstructure and mechanical properties in the thin film system Cu-Zr, Thin Solid Films. 645 (2018) 193–202, https://doi.org/10.1016/j.tsf.2017.10.030.

[29] S.W. Fackler, V. Alexandrakis, D. König, A.G. Kusne, T. Gao, M.J. Kramer, D. Stasak, K. Lopez, B. Zayac, A. Mehta, A. Ludwig, I. Takeuchi, Combinatorial study of Fe-Co-V hard magnetic thin films, Sci. Technol. Adv. Mater. 18 (2017) 231–238, https://doi.org/10.1080/14686996.2017.1287520.

[30] F. Ren, R. Pandolfi, D. Van Campen, A. Hexemer, A. Mehta, On-the-fly data assessment for high-throughput X-ray diffraction measurements, ACS Comb. Sci. 19 (2017) 377–385, https://doi.org/10.1021/acscombsci.7b00015.

[31] S. Pauly, S. Gorantla, G. Wang, U. Kühn, J. Eckert, Transformation-mediated ductility in CuZr-based bulk metallic glasses, Nat. Mater. 9 (2010) 473–477, https://doi.org/10.1038/nmat2767.

[32] K. O'Connell, J.R. Regalbuto, High sensitivity silicon slit detectors for 1 nm powder XRD size detection limit, Catal. Lett. 145 (2015) 777–783, https://doi.org/10.1007/s10562-015-1479-6.

[33] M.C. Rowe, B.J. Brewer, AMORPH: A statistical program for characterizing amorphous materials by X-ray diffraction, Comput. Geosci. 120 (2018) 21–31, https://doi.org/10.1016/j.cageo.2018.07.004.

[34] T. Egami, Y. Tong, W. Dmowski, Deformation in metallic glasses studied by synchrotron X-ray diffraction, Metals (Basel). 6 (1) (2016) 22.

[35] T.A. Baser, M. Baricco, S. Enzo, G. Vaughan, A.R. Yavari, Analysis of crystallization behavior of Fe48Cr15 Mo14Y2 C15B6 bulk metallic glass by

synchrotron radiation, J. Mater. Res. 23 (2008) 2166–2173, https://doi.org/10.1557/jmr.2008.0264.

[36] W. Minor, B. Schonfeld, B. Lebech, B. Buras, W. Dmowski, Crystallization of Fe-Si-B metallic glasses studied by X-ray synchrotron radiation, J. Mater. Sci. 22 (11) (1987) 4144–4152.

[37] I. Kalay, M.J. Kramer, R.E. Napolitano, Crystallization kinetics and phase transformation mechanisms in Cu56Zr44 glassy alloy, Metall. Mater. Trans. A. 46 (8) (2015) 3356–3364.

[38] T. Cullinan, I. Kalay, Y.E. Kalay, M. Kramer, R. Napolitano, Kinetics and mechanisms of isothermal devitrification in amorphous Cu50Zr50, Metall. Mater. Trans. A Phys. Metall. Mater. Sci. 46 (2015) 600–613, https://doi.org/10.1007/s11661-014-2661-y.

[39] K.H. Kang, K.W. Park, J.C. Lee, E. Fleury, B.J. Lee, Correlation between plasticity and other materials properties of Cu-Zr bulk metallic glasses: an atomistic simulation study, Acta Mater. 59 (2011) 805–811, https://doi.org/10.1016/j.actamat.2010.10.027.

[40] D. Xu, B. Lohwongwatana, G. Duan, W.L. Johnson, C. Garland, Bulk metallic glass formation in binary Cu-rich alloy series – Cu100−xZrx (x=34, 36, 38.2, 40 at.%) and mechanical properties of bulk Cu64Zr36 glass, Acta Mater. 52 (9) (2004) 2621–2624.

[41] A.P. Hammersley, S.O. Svensson, M. Hanfland, A.N. Fitch, D. Hausermann, Two-dimensional detector software: from real detector to idealised image or two-theta scan, Int. J. High Press. Res. 14 (1996) 235–248.

[42] X. Qiu, J.W. Thompson, S.J.L. Billinge, PDFgetX2: a GUI driven program to obtain the pair distribution function from X-ray powder diffraction data, J. Appl. Cryst. 37 (2004) 678–678.

[43] J. Bednarčik, S. Michalik, V. Kolesar, U. Rütt, H. Franz, In situ XRD studies of nanocrystallization of Fe-based metallic glass: a comparative study by reciprocal and direct space methods, Phys. Chem. Chem. Phys. 15 (15) (2013) 8470–8479, https://doi.org/10.1039/c3cp44445g.

[44] L. Lutterotti, M. Bortolotti, G. Ischia, I. Lonardelli, H.-R. Wenk, Rietveld texture analysis from diffraction images, Z. Krist. 2007 (suppl_26) (2007) 125–130.

[45] http://pd.chem.ucl.ac.uk/pdnn/diff2/cone.gif, 03.2021. (3AD).

[46] H.E. Swanson, R.K. Fuyat, Circ. 539, Natl. Bur. Stand. II (1953).

[47] J. Rawers, M. R, Private Communication, United States Dept. Inter. Bur. Mines, Albany, Oregon, USA, 1991.

[48] I. Kabana, P. Jóvári, V. Kokotin, O. Shuleshova, B. Beuneu, K. Saksl, N. Mattern, J. Eckert, A.L. Greer, Local atomic arrangements and their topology in Ni–Zr and Cu–Zr glassy and crystalline alloys, Acta Mater. 61 (2013) 2509–2520, https://doi.org/10.1016/j.actamat.2013.01.027.

[49] R. Jana, L. Pastewka, Correlations of non-affine displacements in metallic glasses through the yield transition, J. Phys. Mater. 2 (2019) 045006.

[50] X. Tong, G. Wang, Z. Stachurski, E. Al, Structural evolution and strength change of a metallic glass at different temperatures, Sci Rep. 6 (2016) 30876.

[51] W. Qin, J.A. Szpunar, Y. Umakoshi, A criterion for grain-size limit of polycrystalline materials, J. Appl. Phys. 106 (2009) 10–13, https://doi.org/10.1063/1.3157928.

[52] J.Y. Huang, Y.T. Zhu, X.Z. Liao, R.Z. Valiev, Amorphization of TiNi induced by high-pressure torsion, Philos. Mag. Lett. 84 (2004) 183–190, https://doi.org/10.1080/09500830310001657353.

[53] https://materials.springer.com/isp/crystallographic/docs/sd_0451625, (n.d.).

[54] T. Ungár, G. Tichy, J. Gubicza, R.J. Hellmig, Correlation between subgrains and coherently scattering domains, Powder Diffr. 20 (2005) 366–375, https://doi.org/10.1154/1.2135313.

[55] T. Mei-Bo, Z. De-Qian, P. Ming-Xiang, W. Wei-Hua, Binary Cu–Zr bulk metallic glasses, Chin Phys Lett. 21 (5) (2004) 901–903.

[56] X.D. Wang, S. Yin, Q.P. Cao, J.Z. Jiang, H. Franz, Z.H. Jin, Atomic structure of binary Cu64.5 Zr35.5 bulk metallic glass, Appl. Phys. Lett. 92 (2008) 3–6, https://doi.org/10.1063/1.2828694.

[57] P. Zeman, M. Zítek, Š. Zuzjaková, R. Čerstvý, Amorphous Zr-Cu thin-film alloys with metallic glass behavior, J. Alloys Compd. 696 (2017) 1298–1306.

[58] M. Apreutesei, P. Steyer, L. Joly-Pottuz, A. Billard, J. Qiao, S. Cardinal, F. Sanchette, J.M. Pelletier, C. Esnouf, Microstructural, thermal and mechanical behavior of co-sputtered binary Zr-Cu thin film metallic glasses, Thin Solid Films. 561 (2014) 53–59, https://doi.org/10.1016/j.tsf.2013.05.177.

[59] B.R. Braeckman, D. Depla, On the amorphous nature of sputtered thin film alloys, Acta Mater. 109 (2016) 323–329, https://doi.org/10.1016/j.actamat.2016.02.035.

[60] A. Bartsch, K. Rätzke, A. Meyer, F. Faupel, Dynamic arrest in multicomponent glass-forming alloys, Phys. Rev. Lett. 104 (2010) 1–4, https://doi.org/10.1103/PhysRevLett.104.195901.

[61] D.J. Sordelet, X.Y. Yang, E.A. Rozhkova, M.F. Besser, M.J. Kramer, Oxygen-stabilized glass formation in Zr80Pt20 melt-spun ribbons, Appl. Phys. Lett. 83 (2003) 69–71, https://doi.org/10.1063/1.1588371.

[62] D.J. Sordelet, X. Yang, E.A. Rozhkova, M.F. Besser, M.J. Kramer, Influence of oxygen content in phase selection during quenching of Zr 80Pt20 melt spun ribbons, Intermetallics. 12 (2004) 1211–1217, https://doi.org/10.1016/j.intermet.2004.04.009.

[63] J.R.M.M.J. Kramer, M. Xu, Y.Y. Ye, D.J. Sordelet, Phase stability and transformations in the Zr2NiCu1-x amorphous system, Met. Mater Trans A. 39A (2008) 1847–1856.

[64] C. Prakash, Thermal conductivity variation of silicon with temperature, Microelectron. Reliab. 18 (1978) 333, https://doi.org/10.1016/0026-2714(78)90573-5.

[65] https://www.dupont.com/content/dam/dupont/amer/us/en/products/ei-trans-formation/documents/EI-10142-Kapton-Summary-of-Properties.pdf, (n.d.).

[66] C.Y. Yu, X.J. Liu, J. Lu, G.P. Zheng, C.T. Liu, First-principles prediction and experimental verification of glass-forming ability in Zr-Cu binary metallic glasses, Sci. Rep. 3 (2013) 1–5, https://doi.org/10.1038/srep02124.

[67] L. Xia, S.S. Fang, Q. Wang, Y.D. Dong, C.T. Liu, Thermodynamic modeling of glass formation in metallic glasses, Appl. Phys. Lett. 88 (2006) 2004–2007, https://doi.org/10.1063/1.2198830.

[68] H. Okamoto, Cu-Zr (Copper-Zirconium), J. Phase Equilib. Diffus. 33 (2012) 417–418, https://doi.org/10.1007/s11669-012-0077-1.